Available online at www.sciencedirect.com
SCIENCE DIRECT
ELSEVIER
Earth and Planetary Science Letters 236 (2005) 404–418
EPSL
www.elsevier.com/locate/epsl

In situ cosmogenic ^{10}Be and ^{21}Ne in sanidine and in situ cosmogenic ^{3}He in Fe–Ti-oxide minerals

F. Kober [a,b,*], S. Ivy-Ochs [c,d], I. Leya [b,1], H. Baur [b], T. Magna [b], R. Wieler [b], P.W. Kubik [e]

[a] *Institute of Geology, ETH Zurich, CH-8092 Zurich, Switzerland*
[b] *Institute of Isotope Geology, ETH Zurich, CH-8092 Zurich, Switzerland*
[c] *Institute of Particle Physics, ETH Zurich, CH-8093 Zurich, Switzerland*
[d] *Institute of Geography, University of Zurich, CH-8057 Zurich, Switzerland*
[e] *Paul Scherrer Institute, c/o Institute of Particle Physics, ETH Zurich, CH-8093 Zurich, Switzerland*

Received 22 September 2004; received in revised form 14 April 2005; accepted 3 May 2005
Available online 27 June 2005
Editor: K. Farley

Abstract

We report concentrations of in situ cosmogenic ^{10}Be and ^{21}Ne from coexisting quartz and sanidine separates and of cosmogenic ^{3}He in coexisting Fe–Ti-oxide minerals from ignimbritic successions of northern Chile (Oxaya and Lauca ignimbrites). New mineral-isotope pairs such as sanidine and Fe–Ti-oxide minerals are helpful in quantitative geomorphology for geological settings where the lithology lacks the commonly used minerals quartz, pyroxene or olivine. Production rates in sanidine and Fe–Ti-oxide minerals were determined by normalizing nuclide concentrations to established production rates in quartz. The experimentally determined production rates are compared to model production rates calculated with new cross-sections for ^{3}He, ^{21}Ne, and ^{10}Be production from the individual target elements. The mean experimental ^{21}Ne production rate for five sanidine samples is 30.4 ± 3.7 atoms g^{-1} yr^{-1} (30.4 ± 5.4 atoms g^{-1} yr^{-1} including the uncertainty of the ^{21}Ne production rate in quartz, $P^{21}Ne_{qtz}$). This is in excellent agreement with the modelled value of 28.3 atoms g^{-1} yr^{-1}, which has an estimated uncertainty of 20%. The ^{21}Ne production rate in sanidine is thus about 50% higher than that in quartz. The cosmogenic neon in sanidine is entirely released in low temperature steps (400–600 °C) and no signs of an interfering nucleogenic neon component were observed. This is in stark contrast to quartz and makes sanidine an attractive mineral for terrestrial cosmogenic neon studies. ^{3}He diffuses out of the sanidine structure. Preliminary results also indicate that sanidine is well suited for ^{10}Be studies. The mean experimental ^{10}Be production rate from two sanidine samples is 4.45 ± 0.38 atoms g^{-1} yr^{-1} (4.45 ± 0.42 atoms g^{-1} yr^{-1} including uncertainty of $P^{10}Be_{qtz}$), very close to the modelled value of 4.55 atoms g^{-1} yr^{-1}, which has an estimated uncertainty of 20%. We emphasize that ^{10}Be and ^{21}Ne production in sanidine is composition dependent. Therefore, major element analyses should be carried out and production rates calculated on a sample by sample basis.

* Corresponding author. Institute of Geology, ETH Zurich, CH-8092 Zurich, Switzerland. Tel.: +41 1 6320361.
E-mail address: kober@erdw.ethz.ch (F. Kober).
[1] Present address: Institute of Physics, University of Bern, CH-3012 Bern, Switzerland.

0012-821X/$ - see front matter
doi:10.1016/j.epsl.2005.05.020

Fe–Ti-oxide minerals retain ^{3}He quantitatively. Experimentally derived production rates are in excellent agreement with new values derived from physical modelling. The mean experimental ^{3}He production rate for five Fe–Ti-oxide minerals samples is 120 ± 11 atoms g^{-1} yr^{-1} (120 ± 12 atoms g^{-1} yr^{-1} including the uncertainties of $P^{21}Ne_{qtz}$), compared to a mean modelled value of 124 atoms g^{-1} yr^{-1}, which has an estimated uncertainty of 20%. The variable chemical and structural composition of the solid solution lines of Fe–Ti-oxide minerals has little effect on the total ^{3}He production rate. Cosmogenic ^{21}Ne is not produced in significant quantities in Fe–Ti-oxide minerals due to the absence of suitable target elements.

Keywords: cosmogenic nuclides (^{3}He, ^{10}Be, ^{21}Ne); Fe–Ti-oxide minerals; sanidine; elemental production rates

1. Introduction

Terrestrial cosmogenic nuclides (TCN) such as ^{3}He, ^{10}Be, ^{14}C, ^{21}Ne, ^{26}Al and ^{36}Cl are widely used in Quaternary Geology and Geomorphology for exposure dating and erosion rate estimates (e.g., [1–4]). The minerals most commonly utilized are quartz (^{10}Be, ^{21}Ne, ^{26}Al), pyroxene and olivine (^{3}He, ^{21}Ne). Several studies have shown that quartz can be cleaned reliably of meteoric ^{10}Be [5,6] and retains ^{21}Ne quantitatively [4]. Both pyroxene and olivine have been shown to retain both ^{3}He and ^{21}Ne [7–11]. ^{36}Cl can be measured in any rock type, as whole rock samples are used and the production rate is calculated individually for each sample [3,12]. In many situations, it would be desirable to rely on other minerals, for example if the lithology does not contain the minerals listed above. The search for the optimal samples from a geomorphological perspective would then not be compromised by the need to collect samples with a suitable mineralogy.

^{3}He is especially attractive because it is easily measured due to its high production rates and low detection limits [8,11,13]. Unfortunately, the most commonly used target mineral quartz does not retain ^{3}He [9,14]. Recently, ^{3}He was investigated in garnet [15], although the high U–Th concentrations in the mineral required a careful assessment of the nucleogenic ^{3}He, i.e., ^{3}He produced via the reaction of $^{6}\mathrm{Li}(n,\alpha)\,^{3}\mathrm{H} \rightarrow {}^{3}\mathrm{He}$. ^{3}He-and ^{4}He-studies in magnetite revealed quantitative retention [16–18]. On the other hand, studies by [19,20] indicate that plagioclase retains neither helium nor neon quantitatively.

In this study we explore the usefulness of the mineral sanidine and Fe–Ti-oxide mineral group for exposure dating with cosmogenic noble gases and ^{10}Be. Both minerals can coexist with quartz in silicic volcanic rocks. This allows a reliable cross-calibration, since the production systematics of ^{10}Be, ^{21}Ne and ^{26}Al in quartz are well known [21–28]. We chose seven samples from the ignimbrites of the Oxaya and Lauca Formations of Northern Chile. These rocks contain phenocrysts of quartz, sanidine and Fe–Ti-oxide minerals and are therefore ideally suited to study multiple nuclides in multiple target minerals. Detailed ^{10}Be and ^{21}Ne analyses in quartz samples in these rocks are reported in Kober et al. [29] and summarized in Table A, Background Data Set and Table 2.

We will show below that ^{3}He in Fe–Ti-oxide minerals ($^{3}He_{Fe-Ti}$) and ^{10}Be and ^{21}Ne in sanidine ($^{10}Be_{san}$, $^{21}Ne_{san}$) are well suited for TCN studies. Conversely, $^{3}He_{san}$ and $^{21}Ne_{mt}$ are of little use due to poor retention of cosmogenic ^{3}He ($^{3}He_{c}$) in sanidine and low production rates of cosmogenic ^{21}Ne ($^{21}Ne_{c}$) in Fe–Ti-oxide minerals, respectively. The experimental production rates presented here are compared to results from new model calculations for cosmogenic nuclide production. The modelling is based on new cross-sections for ^{3}He, ^{21}Ne, and ^{10}Be production from the relevant target elements.

2. Mineral aspects

2.1. Sanidine

Sanidine is a high-temperature/low-pressure alkali-feldspar found most commonly in rhyolites, dacites, trachytes and phonolites and less frequently in contact metamorphic rocks. Sanidine can occur both as phenocrysts and in the ground mass. Phenocrysts of sanidine coexist with quartz or can be the sole phenocrystic phase. If sanidine would be a mineral suit-

able for TCN work, isotope studies could be extended to volcanic regions where the rocks lack quartz or pyroxene and where timescales longer than that dictated by ^{36}Cl-saturation are of interest. Compared to plagioclase, alkali-feldspars are more resistant to chemical attack and generally last longer in the sedimentary and soil environment [30–32]. As will be discussed below, the sanidine phenocrysts from the studied ignimbrites appear fresh and contain no incipient clay alteration.

Within the sanidine-lattice, Si and Al are disordered which requires charge balance that is most frequently accomplished with K-or Na-cations. Thus, in contrast to quartz, the major element composition of sanidines from different rocks can differ with respect to the main target elements for ^{10}Be and ^{21}Ne production. The concentrations of the target elements important for the production of cosmogenic neon and beryllium in sanidine are given in Table B, Background Data Set. Note that sample CN104 for beryllium analysis is not pure sanidine but likely contained about 20% of quartz. Furthermore, sanidine has been suggested to retain Ar isotopes due to a less complex lattice [33] compared to plagioclase.

2.2. Fe–Ti-oxide minerals

Fe–Ti-oxide minerals like the endmembers magnetite and ulvospinel (with the solid solution line of titatnomagnetite) and hematite and ilmenite (titanohematites) are very common accessory minerals in igneous and metamorphic rocks [34,35]. The usefulness of Fe–Ti-oxide minerals in TCN studies by studying ^{3}He was suggested by Bryce and Farley [18] using magnetite and lately by Margerison et al. [36] using ilmenite, whereas production of ^{21}Ne is expected to be too low [37].

3. Sample site geology

The analysed samples stem from the Western Escarpment of the northern part of the Atacama Desert and the Western Cordillera in northern Chile. This area is characterized by a hyperarid to arid climate. Active tectonics occurs due to the convergence of the Nazca Plate below the South American continent, leading to uplift of the Andes [38]. The hyperarid climate in the northern branch of the Atacama Desert results in very low erosion rates and hence in very old preserved landscapes [39–42] similar to ice-free regions in Antarctica [11]. Erosion rates at the northern branch of the Atacama Desert derived from cosmogenic nuclide concentrations in quartz are <100 cm/My [29]. The Western Cordillera in turn receives more rainfall and erosion rates may exceed 1000 cm/My [29]. The samples studied are from resistant ignimbrite (welded tuff) units of the volcano-sedimentary Oxaya Formation (early Miocene, 19–25 My) and from the less resistant Lauca Formation (Pliocene, ~2.7My) [43,44]. Nominal exposure ages to cosmic rays (uncorrected for erosion) are in the order of 1–3 My in case of the Oxaya ignimbrite samples and 10–100 ky for the Lauca ignimbrite samples.

The rocks we studied are made up of 40–50% phenocrysts of sanidine, quartz, plagioclase, biotite, Fe–Ti-oxide minerals and hornblende (in order of abundance) set in a matrix of partially devitrified volcanic glass. Some shards are still visible. Both quartz and sanidine are colourless, crystal clear and up to 3 mm in diameter (mean size is about 1–2 mm). Such large grain-sizes indicate that diffussional loss of $^{21}Ne_{cos}$ are negligible [14,45]. The quartz phenocrysts are euhedral but strongly resorbed, with embayed margins, and often contain glass inclusions (i.e., melt inclusions). Sanidine phenocrysts are euhedral and blocky with sharp grain boundaries. They lack any turbid areas which would indicate alteration to clays. Plagioclase phenocrysts are invariably zoned with turbid alteration areas concentrated within specific zones or in the cores. Margins are often irregular. Fe–Ti-oxide minerals occur either as octahedral phenocrysts or as aggregates in altered hornblende and biotite (see also below). The maximum size of Fe–Ti-oxide mineral grains is up to 1 mm, while the mean grain size is ~0.3 mm.

4. Sample preparation and measurement techniques

Rock samples (Oxaya ignimbrite: CN5, CN19, CN23, CN111, CN201; Lauca ignimbrite: CN112, CN113) were crushed and sieved to a grain size range of 355–1000 μm. The crushed rock was then

etched several times with weak HF using a shaker table [6,46]. This served to dissolve the volcanic groundmass, biotite, hornblende and plagioclase, while quartz, sanidine and Fe–Ti-oxide minerals were enriched. Fe–Ti-oxide minerals were separated using magnetic susceptibility. Sanidine and quartz were separated and purified using heavy liquids (sanidine is found in the density fraction ≤ 2.62 g cm^{-3}). Fe–Ti-oxide minerals were analysed by thin section examination and primary oxide minerals were predominately magnetite and ilmenite. Primary biotite and hornblende were markedly altered to a mixture of fine-grained Fe–Ti-oxide minerals. Bulk samples of Fe–Ti-oxide minerals were powdered and mineralogically analysed using a Scintag XDS 2000 X-ray diffractometer. Peak comparison indicates a hematite-like composition with a constant offset likely due to Ti-contents. We have also identified single mineral grains of such composition in the magnetic fraction using electron microprobe analysis on carbon coated thin sections.

For the helium and neon measurements in sanidine, pure mineral separates were hand-picked from the enriched fraction which ensured that all grains with adhering phases (e.g., glass) were removed. The sanidine separates were crushed to ≤ 100 μm and aliquots of 40–80 mg were wrapped in commercial aluminium foil. The Fe–Ti-oxide mineral separates were degassed without further crushing. Noble gases were extracted in steps by incremental heating between 200–1750 °C (details given in data tables) in a molybdenum crucible. Released gases were cleaned in a stainless steel extraction line equipped with Al/Zr-getters (SAES®) and activated charcoal held at the temperature of liquid nitrogen before He and Ne were expanded to a cryogenic pump. Helium and neon were separated by adsorbing neon at 14 K on stainless steel frits and analyzing helium first. After the helium measurements, neon was released from the Cryotrap at 50 K. Noble gas analyses were performed in a non-commercial, all-metal magnetic sector mass-spectrometer (90°, 210 mm radius) equipped with a modified Baur–Signer ion source whose sensitivity is essentially constant over the pressure range relevant for this work [47]. The ion source is equipped with a compressor device that increases the sensitivity compared to a conventional source by factors of 120 and 200 for ^{3}He and ^{21}Ne, respectively [47]. Corrections for isobaric interferences for mass 20 have been applied for $^{40}Ar^{++}$ and $H_2\,{}^{18}O$ but were always less than 2%. No correction for CO_2^{++} on ^{22}Ne was necessary. The low corrections factors for doubly charged species were the results of a low electron acceleration voltage of 45 V in the ion source. Data reduction followed e.g., study by Oberholzer et al. [48]. Helium in the Fe–Ti-oxide minerals was analysed in a small gas fraction only because ^{4}He-concentrations are as high as $10e^{-4}$ cm^{3}STP g^{-1}. In addition, some of the Fe–Ti-oxide minerals samples were measured by online crushing in order to constrain possible contributions from mantle derived ^{3}He. Nucleogenic ^{3}He (via the reaction $^{6}\mathrm{Li}(n,\alpha)^{3}\mathrm{H}\rightarrow{}^{3}\mathrm{He}$) has been estimated using geological sample ages and measured Li, U and Th-concentrations.

For the ^{10}Be analyses, the quartz and the sanidine mineral separates were further etched using weak HF to ensure removal of meteoric ^{10}Be. Next, following procedures similar to those used to prepare quartz [6,46], they were dissolved with concentrated HF after addition of ^{9}Be carrier. Be was separated and purified using anion and cation exchange and selective pH controlled precipitations [46,49]. ^{10}Be/^{9}Be ratios of the samples along with appropriate standards and blanks were measured by accelerator mass spectrometry at the ETH/PSI tandem facility in Zurich [50]. Blanks were on the order of $(1–3)*10^{-14}$ for ^{10}Be/^{9}Be and amounted to a subtraction of less than 4% for the samples discussed here.

Chemical analysis of sanidine samples was performed by ICP-AES at Service d'Analyse des Roches et des Minéraux CRPG-CNRS, Vandoeuvre-lès-Nancy-France). Li and other trace elements in Fe–Ti-oxide minerals were measured by a PlasmaQuadrupole-ICP mass spectrometer at the ETH Isotope Lab facilities.

5. Isotope data and calculation of experimental production rates

5.1. Sanidine

Neon-concentrations of the sanidine samples are summarized in Table 1. Cosmogenic ^{21}Ne was calculated as excess over atmospheric composition (^{21}Ne/^{20}Ne=0.00296; ^{22}Ne/^{20}Ne=0.102; [51]) (Table 1).

Table 1
Neon concentrations and isotopic ratios in sanidine, production rate calculations and comparisons with modeled production rates

Sample	^{20}Ne	$^{21}Ne/^{20}Ne$	$^{22}Ne/^{20}Ne$	$^{21}Ne_{cosmo-san}$ (400+600 °C)	$^{21}Ne_{qtz}$	Factor san/qtz	$P^{21}Ne_{san}$ experimental by $P^{21}Ne_{qtz}=20.3$ (Niedermann [23])	$P^{21}Ne_{san}$ modelled this study	$P^{21}Ne_{san}$ modelled (Masarik [37])
	$*10^{-10}$	$*10^{-3}$	$*10^{-1}$	$*10^{7}$	$*10^{7}$				
(Heating step(°C)/ heating time(min))	(ccSTP/g)			(atoms/g)	(atoms/g)		(atoms/g/yr)	(atoms/g/yr)	(atoms/g/yr)
CN5S-Ne(400,30′)	1.91 ± 0.04	36.79 ± 0.41	1.56 ± 0.01	32.74 ± 0.63	20.01 ± 0.62	1.64 ± 0.06	33.21 ± 3.54	30.15	24.74
CN5S-Ne(600,30′)	1.77 ± 0.04	35.26 ± 0.24	1.50 ± 0.01						
CN5S-Ne(800,20′)	1.59 ± 0.04	4.93 ± 0.13	1.04 ± 0.01						
CN5S-Ne(1750,20′)	4.79 ± 0.11	3.08 ± 0.07	1.03 ± 0.01						
CN19S-Ne(400,30′)	1.65 ± 0.04	42.99 ± 0.35	1.65 ± 0.01	39.97 ± 0.67	32.03 ± 0.48	1.25 ± 0.03	25.33 ± 2.60	28.07	23.46
CN19S-Ne(600,30′)	2.18 ± 0.04	40.90 ± 0.31	1.60 ± 0.01						
CN19S-Ne(800,20′)	1.35 ± 0.03	5.02 ± 0.03	1.08 ± 0.01						
CN19S-Ne(1750,20′)	0.73 ± 0.02	3.69 ± 0.03	1.02 ± 0.01						
CN23S-Ne(600,30′)	3.93 ± 0.07	38.80 ± 0.25	1.56 ± 0.01	37.80 ± 0.77	22.64 ± 0.42	1.67 ± 0.05	33.89 ± 3.51	29.75	24.38
CN23S-Ne(800,30′)	0.81 ± 0.02	5.38 ± 0.06	1.05 ± 0.01						
CN23S-Ne(1750,20′)	1.18 ± 0.02	3.32 ± 0.07	1.03 ± 0.01						
CN113S-Ne(200,30′)	0.46 ± 0.02	3.10 ± 0.13	1.02 ± 0.02	0.66 ± 0.06	0.48 ± 0.06	1.39 ± 0.23	28.14 ± 5.42	26.44	22.7
CN113S-Ne(400,30′)	1.34 ± 0.02	3.77 ± 0.07	1.03 ± 0.01						
CN113S-Ne(600,30′)	0.62 ± 0.01	5.04 ± 0.20	1.06 ± 0.01						
CN113S-Ne(800,20′)	0.46 ± 0.01	3.08 ± 0.13	1.02 ± 0.02						
CN113S-Ne(1750,15′)	0.58 ± 0.01	3.18 ± 0.10	1.02 ± 0.01						
CN201S-Ne(400,30′)	1.29 ± 0.02	46.86 ± 0.34	1.67 ± 0.01	43.58 ± 0.74	28.36 ± 0.81	1.54 ± 0.05	31.19 ± 3.29	27.03	22.56
CN201S-Ne(600,30′)	0.94 ± 0.02	114.69 ± 0.36	2.69 ± 0.01						
CN201S-Ne(800,20′)	0.52 ± 0.01	4.21 ± 0.09	1.04 ± 0.01						
CN201S-Ne(1750,20′)	0.47 ± 0.01	3.31 ± 0.03	1.03 ± 0.01						
						Mean production rate	30.35 ± 3.67	28.29	23.56

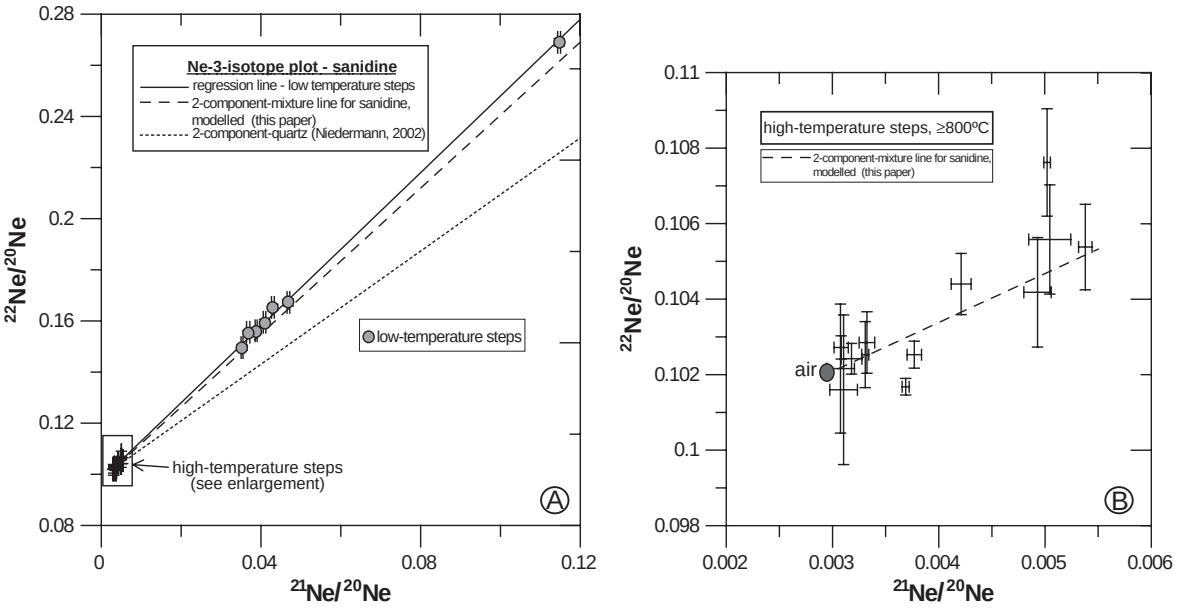

Fig. 1. Neon-three-isotope diagram for sanidine samples. A) All data points of all samples fall on a straight line (solid line) which represents a mixture of atmospheric and cosmogenic composition. Only the low temperature steps (≤600 °C) plot significantly away from atmospheric composition, indicating substantial release of cosmogenic neon. Modeling of a mean sanidine mixing line (dashed line) with new elemental production rates agrees almost perfectly with the regression line through the data points (see text). For reference, the dotted line is a mixing line for quartz [4,23]. B) Enlargement of the area showing the data of high temperature steps (800 and 1750 °C). These steps contain mostly atmospheric Ne and neither major nucleogenic nor trapped contributions.

The neon data are shown in a three-isotope diagram in Fig. 1. Excess $^{21}Ne_c$ was completely released in the 400 °C and 600 °C temperature steps. The 800 °C and total fusion steps showed no significant $^{21}Ne_{excess}$ (Fig. 1B, 2), indicating no significant contributions from nucleogenic or magmatic neon in the high temperature steps. This is in stark contrast to quartz analyses which have shown non-cosmogenic components released in the higher temperature steps [4]. The 800 °C steps always contributed less than 3% of the

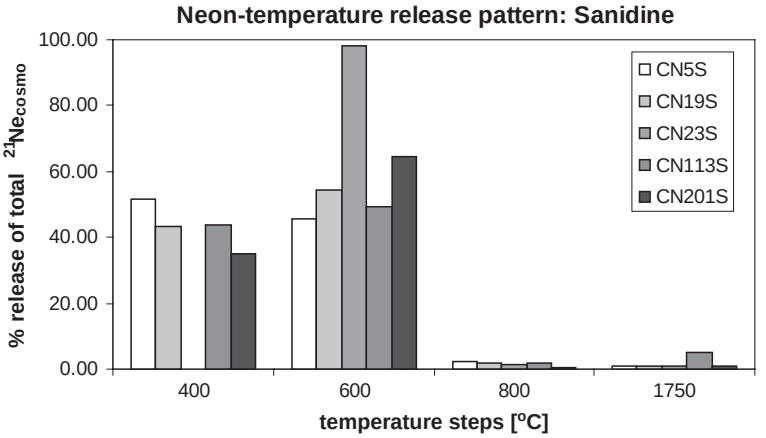

Fig. 2. Percent of released $^{21}Ne_{cosmo}$ at each temperature step relative to total $^{21}Ne_{cosmo}$. For sample CN23S no 400 °C step has been made. 200 °C-step of sample CN113 released 2% and is not shown in graph.

total $^{21}Ne_{excess}$ signature and are not considered here any further. The data of the low temperature steps in Fig. 1a fall on a well-defined straight line ($y=1.4999+0.098$; $R^2=0.9991$). This indicates that all the excess of ^{21}Ne in the 400 and 600 °C steps is entirely cosmogenic. We therefore adopt the sum of the excess ^{21}Ne (over atmospheric composition) in the two low temperature steps as the total cosmogenic ^{21}Ne fraction in the sanidine samples. Note that the regression is almost identical to a mixing line between atmospheric and cosmogenic neon derived from model calculations, as discussed in more detail below.

The experimentally determined ^{21}Ne production rates for sanidine ($^{21}Ne_{san}$) are presented in Table 1. These values were calculated using the nuclide concentration of ^{21}Ne in quartz ($^{21}Ne_{qtz}$) from the same samples determined earlier (Table A, Background Data Set). In order to derive a production rate of $^{21}Ne_{san}$ ($P^{21}Ne_{san}$) for each sample the ratio of ^{21}Ne concentrations ($^{21}Ne_{san}/^{21}Ne_{qtz}$) was multiplied with the $P^{21}Ne_{qtz}=20.3\pm4.0$ atoms g^{-1} yr^{-1} [22,23] at sea level/high latitude. The $P^{21}Ne_{qtz}$ follows a scaling according to Lal [1] (see Table 1 of [23]). This procedure implicitly assumes that the production rate ratios of ^{21}Ne from various elements are independent of altitude and latitude and that ^{21}Ne has been quantitatively retained in both quartz and sanidine. The model calculations below will verify these assumptions for the latitude range of interest here. The mean empirical production rate for ^{21}Ne in sanidine is 30.4 ± 3.7 atoms g^{-1} yr^{-1}. The stated error represents the standard-deviation of the values of the five individual samples and partly the inhomogeneous target element composition (as discussed further down). Including the $P^{21}Ne_{qtz}$ uncertainty [23], the empirical ^{21}Ne production rate for sanidine is 30.4 ± 5.6 atoms g_{mt}^{-1} y^{-1}. The production rate in sanidine is therefore about 50% higher than that in quartz (20.3 ± 4.0 atoms g^{-1} yr^{-1} [22,23]).

Concentrations of ^{3}He in sanidine (Table C, Background Data Set) were all close to the blank values with $^{3}He/^{21}Ne_{cosmo}$ ratios below any reasonable production rate ratio. This indicates that sanidine, like quartz, is not quantitatively retentive for cosmogenic ^{3}He [4,14,52].

Concentrations of ^{10}Be for two sanidine samples are presented in Table 2. Again, we use the ratio of ^{10}Be concentrations in sanidine to quartz and the ^{10}Be production rate of 5.44 ± 0.19 atoms g_{qtz}^{-1} y^{-1} [28] to calculate preliminary ^{10}Be production rates for sanidine. The mean of this value is 4.45 ± 0.38 atoms g^{-1} yr^{-1} (4.45 ± 0.42 atoms g^{-1} yr^{-1} including the $P^{10}Be_{qtz}$ uncertainty). Here, the stated uncertainty represents the error of the mean value. The ^{10}Be production rate in sanidine is thus about 80% as efficient as in quartz.

The fact that the ^{10}Be concentrations measured in both sanidines are on the order of 80% of the ^{10}Be concentrations measured in coexisting quartz, gives confidence that the sanidines had been completely cleaned of meteoric ^{10}Be. This is in contrast to several other minerals besides quartz which have been shown to be difficult to be cleaned of meteoric contaminants [6,53–56]. In case of the studied ignimbrite samples, the lack of meteoric ^{10}Be may be due to the absence of secondary weathering minerals (clay, plagioclase) in sanidine which can take up meteoric ^{10}Be during formation [56].

6. Fe–Ti-oxide minerals

Fe–Ti-oxide minerals were degassed by step-wise heating up to a final temperature of 1750 °C (Tables 3, D, Background Data Set). Both, ^{3}He and ^{4}He, were released simultaneously and over a rather broad temperature interval, usually between 800 and 1400 °C, with only a small percentage of the gas being released

Table 2
Beryllium-concentrations in quartz and sanidine, production rate calculations and comparisons with modeled production rates

Sample	Quartz ^{10}Be	Sanidine ^{10}Be	Factor $^{10}Be_{qtz}/^{10}Be_{san}$	$P^{10}Be$ using $P^{10}Be_{qtz}=5.44$ (Kubik and Ivy-Ochs [28])	$P^{10}Be_{san}$ modeling this study	$P^{10}Be_{san}$ modeling (Masarik [37])
	10^7 atoms/g	10^7 atoms/g		atoms/g/yr	atoms/g/yr	atoms/g/yr
CN19	3.46 ± 0.09	2.68 ± 0.15	0.77 ± 0.05	4.21 ± 0.50	4.50	4.87
CN104	2.22 ± 0.07	1.91 ± 0.13	0.86 ± 0.06	4.69 ± 0.58	4.60	5.08
			Mean	4.45 ± 0.38	4.55	4.98

Table 3
Helium and neon concentrations and ratios in Fe–Ti-oxide samples

Sample	^{3}He	^{4}He	^{3}He/^{4}He	R/R_a	Total ^{3}He	Total $^{21}Ne_{cosmo-qtz}$	$^3He_{Fe-Ti}/^{21}Ne_{qtz}$	P^3He_{Fe-Ti} using $P^{21}Ne_{qtz}=20.3$ (Niedermann [23])
	$*10^{-12}$	$*10^{-6}$	$*10^{-6}$		$*10^9$	$*10^7$		
(Heating step (°C)/ heating time (min))	(ccSTP/g)	(ccSTP/g)			(atoms/g)	(atoms/g)		(atoms/g/yr)
CN5Mt(800,30′)	11.64 ± 0.72	3.52 ± 0.04	3.31 ± 0.21	2.38	1.137 ± 0.053	20.01 ± 0.62	5.68 ± 0.32	115.31 ± 13.21
CN5Mt(1400,30′)	30.68 ± 1.83	4.57 ± 0.05	6.71 ± 0.41	4.83				
CN5Mt(1750,20′)	−0.01 ± 0.04	−0.02 ± 0.02						
CN19Mt(600,30′)	10.69 ± 0.27	36.11 ± 0.64	0.30 ± 0.01	0.21	1.727 ± 0.054	32.03 ± 0.48	5.39 ± 0.19	109.42 ± 11.58
CN19Mt(1000,30′)	20.71 ± 0.53	168.16 ± 3.00	0.12 ± 0.01	0.09				
CN19Mt(1400,30′)	32.09 ± 1.91	37.18 ± 0.44	0.86 ± 0.05	0.62				
CN19Mt(1750,20′)	0.78 ± 0.09	0.54 ± 0.02	1.44 ± 0.17	1.04				
CN23Mt(600,30′)	7.34 ± 0.44	13.17 ± 0.09	0.56 ± 0.03	0.40	1.349 ± 0.045	22.64 ± 0.42	5.96 ± 0.23	120.94 ± 12.94
CN23Mt(800,30′)	3.45 ± 0.23	31.28 ± 0.22	0.11 ± 0.01	0.08				
CN23Mt(1000,30′)	14.24 ± 0.85	29.87 ± 0.21	0.48 ± 0.03	0.34				
CN23Mt(1200,30′)	22.83 ± 1.34	22.61 ± 0.16	1.01 ± 0.06	0.73				
CN23Mt(1400,30′)	1.89 ± 0.13	0.84 ± 0.01	2.23 ± 0.15	1.61				
CN23Mt(1750,20′)	0.47 ± 0.05	0.18 ± 0.01	2.58 ± 0.27	1.86				
CN111Mt(200,30′)	0.04 ± 0.01	0.00 ± 0.01	18.22 ± 2.65	13.11	0.915 ± 0.006	13.42 ± 0. 51	6.82 ± 0.26	138.46 ± 14.85
CN111Mt(400,30′)	0.03 ± 0.01	0.08 ± 0.01	0.46 ± 0.08	0.33				
CN111Mt(600,30′)	1.19 ± 0.03	3.06 ± 0.03	0.39 ± 0.01	0.28				
CN111Mt(800,20′)	1.54 ± 0.03	3.72 ± 0.03	0.41 ± 0.01	0.30				
CN111Mt(1000,20′)	1.94 ± 0.03	2.97 ± 0.02	0.65 ± 0.01	0.47				
CN111Mt(1200,30′)	17.33 ± 0.17	10.55 ± 0.09	1.64 ± 0.02	1.18				
CN111Mt(1400,20′)	11.08 ± 0.12	3.28 ± 0.03	3.38 ± 0.05	2.43				
CN111Mt(1600,15′)	0.90 ± 0.02	0.19 ± 0.01	4.79 ± 0.13	3.45				
CN112Mt(1000,20′)	2.69 ± 0.07	15.25 ± 0.18	0.18 ± 0.01	0.13	0.149 ± 0.002	2.61 ± 0.09	5.71 ± 0.22	115.93 ± 12.42
CN112Mt(1400,20′)	2.79 ± 0.06	7.12 ± 0.08	0.39 ± 0.01	0.28				
CN112Mt(1600,15′)	0.06 ± 0.01	0.11 ± 0.00	0.55 ± 0.11	0.40				
				Mean				120.01 ± 11.09
				P^3He_{Fe-Ti}, mean modelled, this study				124
				P^3He_{mt}, experimental (Bryce and Farley 2002; [18])				69–77
				P^3He_{mt}, modelled (Masarik 2002; [37])				63.5

Helium-3–Fe–Ti production rate calculation and comparison with modelled and experimentally established production rates.

at either lower or higher temperatures. The final temperature steps (1750 °C) contained little gas, suggesting complete degassing at ≤1400 °C (Fig. A, Background Data Set). ^{3}He in all steps of all samples is assumed to be entirely of cosmogenic origin and is used for production rate calculations. As we will show below non-cosmogenic contributions can be neglected.

Similar to sanidine, ^{3}He production rates for Fe–Ti-oxide minerals were calculated by using the ^{21}Ne concentrations of quartz from the same sample (Table A, Background Data Set) and the procedure delineated above. Resulting ^{3}He production rates are presented in Table 3. The mean of 120 ± 11 atoms g_{mt}^{-1} y^{-1} (120 ± 12 atoms g_{mt}^{-1} y^{-1} including the $P^{21}Ne_{qtz}$ uncertainty, [23]) is considerably higher than a previous value obtained from numerical simulations of 63 atoms g_{mt}^{-1} y^{-1} by Masarik [37] or the preliminary experimentally determined value of 69–77 atoms g_{mt}^{-1} y^{-1} of Bryce and Farley [18].

The Ne-three-isotope diagram (Fig. B, Background Data Set) shows that very few data points lie on a mixing line between atmospheric and cosmogenic neon. Therefore no unambiguous contribution of cosmogenic ^{21}Ne can be detected. Excesses over atmospheric composition are likely due to nucleogenic and/or magmatic contributions. We therefore conclude that ^{21}Ne in Fe–Ti-oxide minerals is not useful for exposure dating. We will show below that this is to be

expected based on the low ^{21}Ne production rate from Fe.

Note that the production rates for Fe–Ti-oxide minerals and sanidine reported here are valid essentially for present-day magnetic field intensities although the exposure ages of the samples are in the order of 10 ky to 3 My (see above). This is because we have normalized to the production rate for quartz deduced by Niedermann and Niedermann et al. [22,23] based on samples with exposure ages of 13 ky only that required no correction for changes in the magnetic field intensity at earlier times. According to Masarik et al. [57] these corrections would amount to 9% for the low latitudes samples studied here (20°S) and for samples with exposure >50 ky. The correction for samples <50 ky as established by Dunai [58] for low latitude samples is 15%. This means that the reader should perform corrections for paleofield intensity variations if necessary when adopting the production rates for sanidine and Fe–Ti-oxide minerals recommended here.

7. Modeling of cosmogenic nuclide production rates on Earth

Here we present new modelled cosmogenic production rates for most of the major target elements relevant for TCN-studies. These modeled values (Tables 4, 5—uncertainties estimated in Tables 2 and 3) are based on the particle fluxes in the Earth's atmosphere [59] and the cross-sections for the relevant nuclide reactions. The cross-sections were obtained from various irradiation experiments [60]. The primary model output are elemental production rate ratios relative to Si ([X]/[Si]), where [X] denotes O, Mg, Al, Fe and Ni for helium, [X]=Na, Mg, Al, Ca, Fe and Ni for neon, and [X]=O, N, Mg, Al, Ca, Fe, Ni for beryllium. These ratios are essentially constant at all latitudes and altitudes up to 6000 m, hence in the following we adopt the values modeled for sea level and high latitude. Note that the [X]/[Si] ratios may change considerably at altitudes above 6000 m, but this is hardly relevant in practice. Absolute neon production rates for the specific elements were then obtained by normalizing the model-derived X/[Si]-ratios with the absolute production rate derived by Niedermann and Niedermann et al. [22,23] with quartz samples from the Sierra Nevada ($P^{21}Ne_{Si}$=43.5±8.7 atoms g^{-1} y^{-1} at sea level, high latitude). The estimated uncertainties of the specific elemental production rates are 20%. The elemental P^{21}Ne values for Mg and Al in Table 5A are slightly different from those given by Schäfer et al. [11] due to recently updated cross-sections (see above).

Concerning helium, most of the radioactive ^{3}H ($t_{1/2}$~12.3y) in the artificially irradiated targets studied for cross-section measurements (e.g., [61]) had not yet decayed to ^{3}He by the time the irradiated samples were analysed. Accurate modelling of ^{3}He production rates therefore requires knowledge of the production rate ratio $P(^3He_{direct})/P(^3H)$. We use here the element specific values determined by Leya et al. [61] and earlier by Hintenberger et al. [62,63]: 1.73 [O], 3.0 [Fe], 2.22 [Mg], 2.28 [Al], 2.16 [Si], and 3.0 [Ni]. Data for Ti are assumed to be of the Fe value. These values are considerably different from the ratio of 1 assumed by e.g., paper of Masarik [37], which may explain discrepancies between our elemental production rates and values given by Masarik [37] discussed below. In order to establish absolute ^{3}He production rates, first the modelled ^{3}He/^{21}Ne elemental production ratio (Table 4) was calculated. By using again the accepted absolute production rate of $P^{21}Ne_{Si}$=43.5±8.7 atoms g^{-1} y^{-1} [22,23] the absolute ^{3}He production

Table 4
Elemental production rate calculations for ^{3}He for this work (bold) and comparison to previously modelled ^{3}He production rates

Element	O	Mg	Al	Si	Fe	Ni	Ca
$^3He_{element}/^3He_{Si}$	1.482	1.414	1.244	1.000	0.739	0.707	–
Modelled ratio $(^3He/^{21}Ne)_{Si}$				2.962			
$P^{21}Ne_{Si}$ (atoms/g/yr) (Niedermann [23])				43.5			
P^3He_{Si} (atoms/g/yr)				129			
$P^3He_{element}$ (atoms/g/yr)	**191**	**182**	**160**	**129**	**95**	**91**	–
$P^3He_{element}$ (atoms/g/yr) (Masarik [37])	129	111	102	106	39	–	58

Table 5

A) Model calculations of ^{21}Ne elemental production rates and comparison to previously established elemental production rates

Element	Na	Mg	Al	Si	Ca	Fe	Ni
$^{21}Ne_{element}/^{21}Ne_{Si}$	4.780	4.340	1.371	1.000	0.381	0.019	0.019
$^{21}Ne_{Si}$ (atoms/g/yr) (Niedermann [23])				43.5			
$P^{21}Ne_{element}$ (atoms/g/yr)	**208**	**189**	**60**	**44**	**17**	**1**	**1**
Masarik [37]	102	175	62	42	2	0	–
Schäfer et al. [68]	–	196	54	45	–	–	–

B) Model calculations of ^{10}Be elemental production rates and comparison to previously established elemental production rates

Element	O	N	Mg	Al	Si	Ca	Fe	Ni
$^{10}Be_{element}/^{10}Be_{Si}$	1.992	7.458	0.588	0.492	1.000	0.340	0.567	0.442
Modelled ratio $(^{10}Be/^{21}Ne)_{Si}$					0.075			
$P^{21}Ne_{Si}$ (atoms/g/yr) (Niedermann [23])					43.5			
Absolute $P^{10}Be$ for Si (atoms/g/yr)					3.28			
$P^{10}Be_{element}$ (atoms/g/yr)	**6.54**	**24.49**	**1.93**	**1.61**	**3.28**	**1.12**	**1.86**	**1.45**
Masarik [37]	9.82	–	1.74	1.03	0.89	–	0.35	–

rate from Si was obtained and the production rates for the other elements of interest were determined via the earlier X/[Si]-ratios.

The mean modelled total ^{21}Ne production rate for sanidine is 28.3 atoms g^{-1} y^{-1} (Table 1). This value refers to the mean major element composition of the sanidine samples analyzed here (Table B, Background Data Set). Similarly, the mean modelled total ^{3}He production rate in Fe–Ti-oxide minerals is 124 atoms g^{-1} y^{-1} (Table 3) using the end-members ulvospinel (Fe_2TiO_4; 124 atoms g^{-1} y^{-1}), ilmenite ($FeTiO_3$; 127 atoms g^{-1} y^{-1}), magnetite (Fe_3O_4; 122 atoms g^{-1} y^{-1}) and hematite (Fe_2O_3; 124 atoms g^{-1} y^{-1}). Hereby it is assumed that the ^{3}He production from titanium and iron does not vary significantly ($P^3He_{Ti} = 1.05 * P^3He_{Fe}$, determined by interpolation between the elemental production from Fe and Si). Therefore, the ^{3}He production rate of Fe–Ti-oxide minerals is essentially independent of the chemical composition.

The mean modelled production rate for ^{10}Be in sanidine is 4.55 atoms g^{-1} y^{-1} (Table 2), including the production by stopped and fast muons following the procedures by Heisinger et al. and Kubik and Ivy-Ochs [26–28]. The considerable differences in the elemental production rate ratios between our new results and the data published by Masarik are most likely due to the different cross-sections used for modeling. For example, the usual assumption of equal cross-sections for proton-and neutron-induced production of ^{10}Be from oxygen is generally not valid [64] and can result in production rates too low by up to a factor of 2. While our calculations are based on neutron-induced cross-sections adjusted to experimental data from physical model calculations [60], the approach by Masarik is mostly based on the assumption of equal cross-sections.

8. Comparison of experimental and modelled production rates

8.1. Sanidine–neon

The sanidine samples studied here all yield experimentally derived ^{21}Ne production rates between 25–34 atoms g^{-1} y^{-1} (Table 1), with a mean of 30.4 ± 3.7 atoms g^{-1} y^{-1}. It is suggested that sanidine retains cosmogenic neon quantitatively. This suggestion is corroborated by the fact that for each sample the model-derived production rate based on the actual chemical composition (ranging from 26–30 atoms g^{-1} y^{-1}, with a mean of 28.29 atoms g^{-1} y^{-1}, Table B, Background Data Set) agrees within uncertainties with the empirically determined value. Hence, the variations of the empirically derived values are to a large extent explainable by variable chemical compositions. The mean production rate for sanidine derived here is considerably higher than the P^{21}Ne value of 20.3 ± 4.0 atoms g^{-1} y^{-1} for quartz [22,23]. This is to be expected, because Na and Al are major elements in sanidine. ^{21}Ne production rates from

these elements are ~1.5 and 5 times higher, respectively, than for Si (Table 5A).

Elemental production rates for ^{21}Ne reported by Masarik [37] would underestimate the total production rate for sanidine by ~20%. Higher elemental production rates for Mg and Al were proposed by Schäfer et al. [11], while a new Na value is provided in this study.

Based on our model we can also calculate the isotopic composition of cosmogenic neon in sanidine (elemental production rates of ^{20,22}Ne in sanidine are not shown in Tables 1, 5A; see Leya et al. [61]). The mixing line between atmospheric and cosmogenic composition in Fig. 1 has been determined using the average chemical composition of the sanidine samples (Table B, Background Data Set) and experimentally determined production rates given in Table 5 by Leya et al. [61]. The modelled line agrees very well with the regression line defined by the data points. This supports the conclusion that apart from atmospheric neon, the bulk of the cosmogenic neon is released in the 400–600 °C steps. Note that the regression line defined by the data points and the modelled line for sanidine is steeper in Fig. 1 compared to the mixing line for quartz [22,23]. This is due to elevated ^{22}Ne/^{21}Ne ratios from both Na and Al compared to Si [61].

8.2. Sanidine–Beryllium

The measured and modelled ^{10}Be production rates reported here agree very well with each other (4.45 ± 0.38 versus 4.55 atoms g^{-1} y^{-1}, Tables 2, 5B). Our modelled value is some 11% lower than if calculated by using elemental production rates given by Masarik [37](Table 5B). Using our elemental production rates given in Table 5B for the calculation of the production rate of ^{10}Be in quartz yields 5.02 atoms g^{-1} y^{-1} (5.65 atoms g^{-1} y^{-1} when following the procedure of Masarik [37]). This is a ~10% lower production rate of ^{10}Be-production in sanidine compared to quartz.

8.3. Fe–Ti-oxide minerals–Helium

Measured ^{3}He production rates for the Fe–Ti-oxide samples are given in Table 3. Values range between 109–138 atoms g_{mt}^{-1} y^{-1}, with a mean of 120 ± 11 atoms g_{mt}^{-1} y^{-1}. As it was the case for neon in sanidine, this mean value is very similar to the modelled $P^3He_{Fe-Ti} = 124$ atoms g_{mt}^{-1} y^{-1} (see section 'Modeling of terrestrial cosmogenic production rates on Earth'). This excellent agreement strongly suggests that our basic assumption is correct that the measured ^{3}He in all samples is essentially cosmogenic. Nevertheless, before we further discuss this value we will first evaluate the possibility that sizeable fractions of ^{3}He are of non-cosmogenic origin. The main reasons for this exercise are that one of our samples (CN111) has a ~15% higher measured production rate than both the modelled and the mean measured values and that our recommended value is considerably higher than the recently proposed P^3He_{Fe-Ti} values of 69–77 atoms g_{mt}^{-1} y^{-1} [18].

Li-concentrations in the Fe–Ti-oxide minerals are in the sub-ppm range (Table E of Appendix A). Assuming for the ignimbrites mean U–Th values similar to average granitic crust [65] and using a ^{3}He production rate of $6*10^{-10}$ atoms g_{mt}^{-1} s^{-1} for 1 ppm of Li [66,67], we conclude that the nucleogenic ^{3}He concentrations are lower than $2*10^5$ atoms g_{mt}^{-1} in the Lauca sample (CN112) and lower than $8.2*10^4$–$6*10^5$ atoms g_{mt}^{-1} for all Oxaya-ignimbrite samples. Sample CN111 in particular does not contain more than $8.2*10^4$ atoms g_{mt}^{-1} of nucleogenic ^{3}He. Nucleogenic ^{3}He does amount to less than 1% of the total measured ^{3}He in any sample and can therefore be ignored.

^{3}He of magmatic origin cannot a priori be excluded. We therefore thoroughly crushed three of our samples in an online crushing device [68]. After 30 to 45 strokes the average grain size had been reduced to a few tenths of microns. Nevertheless, only ~1% (Table F) of the total ^{3}He found in the aliquots analysed by stepwise-heating had been released by crushing, with the ^{3}He/^{4}He-ratios being similar in crushing and heating experiments. This indicates that Fe–Ti-oxide minerals contain at best negligible amounts of magmatic helium. The experiments show further that by very thorough crushing small fractions of cosmogenic helium might be released. Possibly, friction-induced heating locally resulted in temperatures above the threshold for the release of cosmogenic helium.

Traces of other major elements and Ti contents determined in the Fe–Ti-oxide samples used here are shown in Table E and production rates for these

elements are presented in Table 4. The contribution (mostly from Mg and Al) to the total Fe–Ti-oxide minerals production rate is 1 to 3%, which we therefore neglect.

We conclude that neither magmatic nor nucleogenic helium significantly contribute to the total measured helium concentrations in our ignimbrite Fe–Ti-oxide minerals. Therefore cosmogenic ^{3}He in Fe–Ti-oxide minerals is ideally suited for TCN-studies, as long as magmatic or nucleogenic ^{3}He can be excluded or at least accurately corrected for.

Both measured and modelled ^{3}He production rates in Fe–Ti-oxide minerals presented in this work are considerably higher than recently measured values in Bryce and Farley [18] or Margerison et al. [36]. Our $P^{3}He_{Fe-Ti}$ values are also almost twice as high as those calculated with elemental production rates recommended by Masarik [37]. We believe, that our values are to be preferred over previously suggested ones, because of updated cross-sections, and in particular, due to the newly evaluated branching ratios $P(^{3}He_{direct})/P(^{3}H)$. All our experimental values are close to each other and the mean measured value is in excellent agreement with the modelled ratio. However, at present we have no clear explanation for the difference between our values and the preliminary measured production rate suggested by Bryce and Farley [18] and the ones recently suggested by Margerison et al. [36]. We note that the value by Bryce and Farley [18] is based on a cross calibration of their magnetite data with $P^{3}He$ data from Antarctic pyroxenes by Schäffer et al. [11]. It has recently been suggested, however, that not all pyroxene varieties retain cosmogenic ^{3}He quantitatively, since $^{3}He_{cos}/^{21}Ne_{cos}$ ratios vary considerably more than can be explained by variable chemical composition of the targets [69]. We also note that the poorly constrained ^{3}He production rate from Ti and other elements in trace concentration cannot be the reason for the difference between our production rates and the ones by Bryce and Farley [18]. Even assigning a conservative uncertainty of 20% on the modelled production rates would only lead to an approximation of the two production rates. Clearly, more work is necessary on this topic.

Using the new elemental production rates derived here (Table 3), a production rate of ^{3}He in quartz of 162 atoms g_{qtz}^{-1} y^{-1} is calculated (compared to 118 atoms g_{qtz}^{-1} y^{-1} using elemental production rates proposed by Masarik [37]). This value is of importance for experiments with artificial quartz targets exposed in vacuum containers, e.g., for scaling experiments of terrestrial cosmogenic nuclides with latitude and altitude.

The elemental production rates in Table 4 are also of interest for minerals such as olivine and pyroxene. Table 4 suggests that specific mineral production rates are considerably more variable than previously assumed (e.g., paper by Laughlin et al. [70]). For various end-members of the pyroxene group, our model and that by Masarik [37] yield ^{3}He production rates between 135–171 atoms g^{-1} y^{-1} and 91–118 atoms g^{-1} y^{-1}, respectively. For the olivine end-members fayalite and forsterite the range of modelled values is even wider. Our model predicts $P^{3}He$ between 130 and 175 atoms g^{-1} y^{-1}, compared to Masarik's values of 76 and 118 atoms g^{-1} y^{-1}.

Even taking into account the quite considerable uncertainties of the model predictions (20% for the model used here), the two models are thus not consistent with each other. Unfortunately, experimentally determined $P^{3}He$ values for pyroxenes and olivines do not allow to prefer one model prediction over the other, since the experimental values of (99–148 atoms g^{-1} y^{-1}, in Niedermann and Liccardi et al. [4,71] and references therein) are bracketed by the model predictions. Reasons for the difficulty to assess the model quality are that the chemical composition of the analysed pyroxenes and olivines has rarely been reported in detail, other samples may have been biased by pressure anomalies at the sites (e.g., paper by Ackert et al. [72]).

The olivine (and the few available pyroxene) data do thus not allow to prefer one model prediction over the other. Future cosmogenic nuclide studies on olivines and pyroxenes should report the chemical composition in detail to allow evaluation of this problem.

9. Conclusions

We have shown with ignimbrite samples from northern Chile that cosmogenic ^{3}He in Fe–Ti-oxide minerals and ^{21}Ne in sanidine are well retained. We also show the first ^{10}Be data on two sanidine samples,

which indicate that meteoric ^{10}Be can quantitatively be removed by a procedure similar to that used for quartz. Therefore, sanidine is also well suited to be analysed for cosmogenic ^{10}Be. With this study, Fe–Ti-oxide minerals and sanidine can thus be added to the list of minerals suitable for terrestrial cosmogenic nuclide studies. We found a striking agreement between experimentally determined nuclide production rates and values derived from numerical modelling. This confirms that both, experimentally derived production rates and the model calculations are reliable. The helium model calculations here are based on new values for the branching ratios of $P(^3He_{direct})/(P(^3H)$ which for most elements differ considerably from the value of 1 often used in previous studies. The new branching ratios and the improved cross-sections thus yield considerably different production rates of cosmogenic ^{3}He. The calculations also illustrate the importance of knowledge of the major element concentrations for target minerals with more variable composition than quartz. The reason for the discrepancy between our experimental and modelled P^3He compared to previous estimates has not yet been satisfactorily resolved.

In our ignimbrite samples, three mineral phases (quartz, sanidine, Fe–Ti-oxide minerals) and five different nuclides (^{3}He, ^{10}Be, ^{14}C, ^{21}Ne, ^{26}Al) have been analysed in several rock samples. All these nuclides have different production rates and the radionuclides have different half-lifes, therefore they respond differently to production, accumulation and/or decay of nuclides. Together the different nuclides can deliver basic information on exposure times and erosion rates over a broad range of time scales.

Acknowledgements

This study was funded by Swiss National Science Foundation grant 620-576.663 to F. Schlunegger whose support we acknowledge. J. Masarik and S. Niedermann are thanked for discussion of an earlier draft of this manuscript. G. Wörner is acknowledged for providing U/Th data. P. Meister and E. Reusser supported the X-ray and Electron Microsope analysis. This paper benefited from thorough reviews by D. Shuster and an anonymous reviewer. The Zurich AMS facility is jointly operated by the Swiss Federal Institute of Technology, Zurich and the Paul Scherrer Institute, Villigen, Switzerland.

Appendix A. Supplementary data

Supplementary data associated with this article can be found, in the online version, at doi:10.1016/j.epsl.2005.05.020.

References

[1] D. Lal, Cosmic ray labelling of erosion surfaces: in situ nuclide production rates and erosion models, Earth Planet. Sci. Lett. 104 (1991) 424–439.
[2] P.R. Bierman, Using in situ cosmogenic isotopes to estimate rates of landscape evolution: a review from the geomorphologic perspective, J. Geophys. Res. 48 (1994) 386–389.
[3] J.C. Gosse, F.M. Phillips, Terrestrial in situ cosmogenic nuclides: theory and application, Quat. Sci. Rev. 20 (2001) 1475–1560.
[4] S. Niedermann, Cosmic-ray-produced noble gases in terrestrial rocks: dating tools for surface processes, in: D. Porcelli, C.J. Ballentine, R. Wieler (Eds.), Noble Gases in Geochemistry and Cosmochemistry, Reviews in Mineralogy and Geochemistry, vol. 47, 2002, pp. 731–784.
[5] E.T. Brown, J.M. Edmond, G. Raisbeck, F. Yiou, M.D. Kurz, E.J. Brook, Examination of surface exposure ages of Antarctic moraines using ^{10}Be and ^{26}Al, Geochim. Cosmochim. Acta 55 (1991) 2269–2283.
[6] C.P. Kohl, K. Nishiizumi, Chemical isolation of quartz for measurement of in situ-produced cosmogenic nuclides, Geochim. Cosmochim. Acta 56 (1992) 3583–3587.
[7] M.D. Kurz, Cosmogenic helium in a terrestrial rock, Nature 320 (1986) 435–439.
[8] M.D. Kurz, In situ production of terrestrial cosmogenic helium and some applications to geochronology, Geochim. Cosmochim. Acta 50 (1986) 2855–2862.
[9] T.E. Cerling, Dating geomorphologic surfaces using cosmogenic ^{3}He, Quat. Res. 33 (1990) 148–156.
[10] T.E. Cerling, R.J. Poreda, S.L. Rathburn, Cosmogenic ^{3}He and ^{21}Ne age of the big lost river flood, Snake River plain, Idaho, Geology 22 (1994) 227–230.
[11] J.M. Schäfer, S. Ivy-Ochs, R. Wieler, I. Leya, H. Baur, G.H. Denton, C. Schlüchter, Cosmogenic noble gas studies in the oldest landscape on earth: surface exposure ages of the Dry Valleys, Antarctica, Earth Planet. Sci. Lett. 167 (1999) 215–226.
[12] F.M. Phillips, B.D. Leavy, N.O. Jannik, D. Elmore, P.W. Kubik, The accumulation of cosmogenic chlorine-36 in rocks: a method for surface exposure dating, Science 231 (1986) 41–43.
[13] H. Craig, R.J. Poreda, Cosmogenic ^{3}He in terrestrial rocks: the summit lavas of Maui, Proc. Natl. Acad. Sci. U. S. A. 83 (7) (1986) 1970–1974.

[14] T.W. Trull, M.D. Kurz, W.J. Jenkins, Diffusion of cosmogenic ^{3}He in olivine and quartz: implications for surface exposure dating, Earth Planet. Sci. Lett. 103 (1991) 241–256.
[15] E. Gayer, R. Pik, J. Lave, C. France-Lanord, D.L. Bourles, B. Marty, Cosmogenic ^{3}He in Himalayan garnets indicating an altitude dependence of the ^{3}He/^{10}Be production ratio, Earth Planet. Sci. Lett. 229 (1–2) (2004) 91–104.
[16] F.P. Fanale, J.L. Kulp, The helium method and the age of the Cornwall, Pennsylvania magnetite ore, Econ. Geol. 57 (1962) 735–746.
[17] R. Bähr, H.J. Lippolt, R.S. Wernicke, Temperature-induced ^{4}He degassing of specularite and botryoidal hematite: a ^{4}He retentivity study, J. Geophys. Res. 99 (B9) (1994) 17695.
[18] J.G. Bryce, K.A. Farley, ^{3}He exposure dating of magnetite, in: F.A. Podosek (Ed.), Goldschmidt Conference, Geochim. Cosmochim. Acta, vol. 66 (15A), 2002, p. A108, Davos, Switzerland.
[19] D.D. Bogard, P.J. Cressy, Spallation production of ^{3}He, ^{21}Ne and ^{38}Ar from target elements in the Bruderheim chondrite, Geochim. Cosmochim. Acta, 37 (1973) 527–546.
[20] L.A. Bruno, H. Baur, T. Graf, C. Schlüchter, P. Signer, R. Wieler, Dating of Sirius group tillites in the Antarctic Dry Valleys with cosmogenic ^{3}He and ^{21}Ne, Earth Planet. Sci. Lett., 147 (1997) 37–54.
[21] K. Nishiizumi, J.R. Kohl, J.R. Arnold, J. Klein, D. Fink, R. Middleton, Cosmic ray produced ^{10}Be and ^{26}Al in Antarctic rocks: exposure and erosion history, Earth Planet. Sci. Lett., 104 (1991) 440–454.
[22] S. Niedermann, T. Graf, J.S. Kim, K. Kohl, K. Nishiizumi, Cosmic-ray-produced ^{21}Ne in terrestrial quartz: the neon inventory of Sierra Nevada quartz separates, Earth Planet. Sci. Lett., 125 (1994) 341–355.
[23] S. Niedermann, The ^{21}Ne production rate in quartz revisited, Earth Planet. Sci. Lett., 183 (2000) 361–364.
[24] J.O. Stone, G.L. Allan, L.K. Fifield, R.G. Cresswell, Cosmogenic chlorine-36 from calcium spallation, Geochim. Cosmochim. Acta, 60 (1996) 555–561.
[25] J. Stone, Air pressure and cosmogenic isotope production, J. Geophys. Res., 105 (2000) 23753–23759.
[26] B. Heisinger, D. Lal, A.J. Jull, S. Ivy-Ochs, S. Neumaier, K. Knie, V. Lazarev, E. Nolte, Production of selected cosmogenic radionuclides by muons: 1. Fast muons, Earth Planet. Sci. Lett., 200 (2002) 345–355.
[27] B. Heisinger, D. Lal, A.J. Jull, P.W. Kubik, S. Ivy-Ochs, K. Knie, E. Nolte, Production of selected cosmogenic radionuclides by muons: 1. Capture of negative muons, Earth Planet. Sci. Lett., 200 (2002) 357–369.
[28] P.W. Kubik, S. Ivy-Ochs, A re-evaluation of the 0–10 ky ^{10}Be production rate for exposure dating obtained from the Köfels (Austria) landslide, Nucl. Instr. Methods Phys. Res., B, 223–224 (2004) 618–622.
[29] F. Kober, F. Schlunegger, S. Ivy-Ochs, H. Baur, R. Wieler, P.W. Kubik, H. Schneider, Cosmogenic nuclide studies and geomorphological implications in the hyperarid central Western Andes, Northern Chile, in: P.W. AGU (Ed.), AGU Fall Meeting 2003, EOS Transactions, San Francisco, 2003.
[30] A.E. Blum, L.L. Stillings, Feldspar dissolution kinetics, in: A.F. White, S.L. Brantley (Eds.), Chemical Weathering Rates in Silicate Minerals, Reviews in Mineralogy, vol. 31, Min. Soc. America, 1995, pp. 291–346.
[31] H.W. Nesbitt, C.M. Fedo, G.M. Young, Quartz and Feldspar stability, steady and non-steady-state weathering, and petrogenesis of siliciclastic sands and muds, J. Geol. 105 (1997) 173–191.
[32] A.F. White, T.D. Bullen, M.S. Schulz, A.E. Blum, T.G. Huntington, N.E. Peters, Differential rates of feldspar weathering in granitic regoliths, Geochim. Cosmochim. Acta 65 (6) (2001) 847–869.
[33] I. Parsons, D.C. Rex, P. Guise, A.N. Halliday, Argon-loss by alkali feldspars, Geochim. Cosmochim. Acta 52 (1988) 1097–1112.
[34] B.R. Frost, Stability of oxide minerals in metamorphic rocks, in: D.H. Lindsley (Ed.), Oxide Minerals: Petrologic and Magnetic Significance, vol. 25, Mineralogical Society of America, 1991, pp. 469–488.
[35] B.R. Frost, D.H. Lindsley, Occurrence of iron–titanium oxides in igneous rocks, in: D.H. Lindsley (Ed.), Oxide Minerals: Petrologic and Magnetic Significance, Mineralogical Society of America, 1991, pp. 433–468.
[36] H.R. Margerison, W.M. Phillips, F.M. Stuart, G.E. Sudgen, Cosmogenic ^{3}He concentrations in ancient flood deposits from the Coombs Hills, northern Dry Valleys, East Antarctica: interpreting exposure ages and erosion rates, Earth Planet. Sci. Lett. (2004)1991.
[37] J. Masarik, Numerical simulation of in situ production of cosmogenic nuclides, Geochim. Cosmochim. Acta 66 (15A) (2002) A491.
[38] B.L. Isacks, Uplift of the central Andean plateau and bending of the Bolivian orocline, J. Geophys. Res. 93 (1988) 3211–3231.
[39] C. Mortimer, Drainage evolution in the Atacama Desert of northernmost Chile, Rev. Geol. Chile 11 (1980) 3–28.
[40] K. Nishiizumi, R. Finkel, G. Brimhall, T. Mote, G. Mueller, E. Tidy, Ancient exposure ages of alluvial fan surfaces compared with incised stream beds and bedrock in the Atacama Desert of North Chile, GSA Annual Meeting, p. 11402, Toronto.
[41] G. Wörner, D. Uhlig, I. Kohler, H. Seyfried, Evolution of the Western Andean Escarpment at 18°S (N. Chile) during the last 25 Ma: uplift, erosion, and collapse through time, Tectonophysics 345 (2002) 183–198.
[42] F. Kober, F. Schlunegger, G. Zeilinger, H. Schneider, Surface uplift and climate change: the geomorphic evolution of at the western escarpment of the Andes of northern Chile between the Miocene and present, in: S. Willet, N. Hovius, D. Fisher, M. Brandon, (Eds.), Tectonics, Climate and Landscape Evolution GSA- Penrose Special Paper, in press.
[43] G. Wörner, K. Hammerschmidt, F. Henjes-Kunst, J. Lezaun, H. Wilke, Geochronology (^{40}Ar/^{39}Ar, K–Ar and He-exposure ages) of Cenozoic magmatic rocks from northern Chile (18–22°S): implications for magmatism and tectonic evolution of the central Andes, Rev. Geol. Chile 27 (2000) 205–240.

[44] M. García, Evolution Oligo-Miocène de l'Altiplano occidental (arc et avant-arc du nord du Chili, Arica): Tectonique, volcansime, sédimentation, géomorphologie et bilan érosion-sédimentation, Géologie Alpine, Mémoire H.S., vol. 40, 2002.

[45] D.L. Shuster, K.A. Farley, Diffusion kinetics of proton-induced ^{21}Ne, ^{3}He and ^{4}He in quartz, Geochim. Cosmochim. Acta 69 (9) (2005) 2349–2359.

[46] S. Ivy-Ochs, The dating of rock surface using in situ produced ^{10}Be, ^{26}Al and ^{36}Cl, with examples from Antarctica and the Swiss Alps, PhD, 11763, ETH-Zürich, 1996.

[47] H. Baur, A noble-gas mass spectrometer compressor source with two orders of magnitude improvement in sensitivity, in: C. AGU (Ed.), AGU Fall meeting, EOS Transactions, San Francisco, 1999, 80 pp. supplement.

[48] P. Oberholzer, C. Baroni, J.M. Schäfer, J. Orombelli, S. Ivy-Ochs, P.W. Kubik, H. Baur, R. Wieler, Limited Pliocene/Pleistocene glaciation in Deep Freeze Range, northern Victoria Land, derived from in situ cosmogenic nuclides, Antarct. Sci. 15 (4) (2003) 493–502.

[49] D. Child, G. Elliot, C. Mifsud, A.M. Smith, D. Fink, Sample processing for earth science studies at ANTARES, Nucl. Instrum. Methods Phys. Res., B 172 (2000) 856–860.

[50] H.-A. Synal, G. Bonani, M. Doebeli, R.M. Ender, P. Gartenmann, P.W. Kubik, C. Schnabel, M. Suter, Status report of the PSI/ETH AMS facility, Nucl. Instrum. Methods Phys. 123 (1997) 62–68.

[51] P. Eberhardt, O. Eugster, K. Marti, A redetermination of the isotopic composition of atmospheric neon, Z. Naturforsch. 20a (1965) 623–624.

[52] E.J. Brook, M.D. Kurz, Surface-exposure chronology using in situ ^{3}He in Antarctic quartz sandstone boulders, Quat. Res. 39 (1993) 1–10.

[53] J. Klein, R. Giegengack, R. Middleton, P. Sharma, J. Underwood, R.A. Weeks, Revealing histories of exposure using in situ produced ^{26}Al and ^{10}Be in Lybian Desert glass, Radiocarbon 28 (1986) 547–555.

[54] M. Zreda, Development and Calibration of the ^{36}Cl Surface Exposure Dating Method and its Application to the Chronology of Late Quaternary Glaciations, PhD, New Mexico Institute of Mining and Technology, 1994.

[55] M.A. Seidl, R.C. Finkel, M.W. Caffee, G.B. Hudson, W.E. Dietrich, Cosmogenic isotope analysis applied to river longitudinal profile evolution: problems and interpretations, Earth Surf. Processes Landf. 22 (1997) 195–209.

[56] S. Ivy-Ochs, P.W. Kubik, J. Masarik, R. Wieler, L. Bruno, C. Schlüchter, Preliminary results on the use of pyroxene for ^{10}Be surface exposure dating, Schweiz. Mineral. Petrogr. Mitt. 78 (1998) 375–382.

[57] J. Masarik, M. Frank, J.M. Schäfer, R. Wieler, Correction of in situ cosmogenic nuclide production rates for geomagnetic field intensity variations 800,000 years, Geochim. Cosmochim. Acta 65 (17) (2001) 2995–3003.

[58] T.J. Dunai, Influence of secular variation of the geomagnetic field on production rates of in situ produced cosmogenic nuclides, Earth Planet. Sci. 193 (2001) 197–212.

[59] J. Masarik, J. Beer, Simulation of particle fluxes and cosmogenic nuclide production in the Earth's atmosphere, J. Geophys. Res. 104 (D10) (1999) 12099–12111.

[60] I. Leya, H.-J. Lange, S. Neumann, R. Wieler, R. Michel, The production of cosmogenic nuclides in stony meteoroids by galactic cosmic ray particles, Meteorit. Planet. Sci. 35 (2000) 259–287.

[61] I. Leya, F. Begemann, H.W. Weber, R. Wieler, R. Michel, Simulation of the interaction of galactic cosmic ray protons with meteoroids—on the ^{3}H and light noble gas isotopes in isotropically irradiated thick gabbro and iron targets, Meteorit. Planet. Sci. 39 (3) (2004) 367–386.

[62] H. Hintenberger, H. Wänke, Helium-und Neonisotope in Eisenmeteoriten, Z. Naturforsch. 19 (1964) 210–218.

[63] H. Hintenberger, L. Schultz, H. Wänke, H. Weber, Helium-und Neonisotope in Eisenmeteoriten und der Tritiumverlust in Hexaedriten, Z. Naturforschung 22 (1967) 780–787.

[64] R. Michel, M. Gloris, S. Neumann, I. Leya, Neutron cross sections for physical model calculations of cosmogenic nuclide production rates, Meteorit. Planet. Sci. 33 (1998) A108.

[65] M. Mamani, G. Wörner, P. Ruprecht, G. Hartmann, K. Simon, Sources of Central Andean Magmatism in Time and Space: Implications from Geochemical Data from Quaternary to Miocene Volcanism in S. Peru and N. Chile, IAVCEI, Pucon Chile, 2004.

[66] J.N. Andrews, The isotopic composition of radiogenic helium and its use to study groundwater movement in confined aquifers, Chem. Geol. 49 (1985) 339–351.

[67] D. Lal, Production of ^{3}He in terrestrial rocks, Chem. Geol. 66 (1987) 89–98.

[68] J.M. Schäfer, H. Baur, G.H. Denton, S. Ivy-Ochs, D.R. Marchant, C. Schlüchter, R. Wieler, The oldest ice on Earth in Beacon Valley, Antarctica: new evidence from surface exposure dating, Earth Planet. Sci. 179 (2000) 91–99.

[69] P. Oberholzer, Reconstructing Paleoclimate and Landscape History in Antarctica and Tibet with Cosmogenic Nuclides, PhD 15472, ETH, 2004.

[70] A.W. Laughlin, J. Poths, H.A. Healey, S.L. Reneau, D. WoldeGabriel, Dating of Quaternary basalts using the cosmogenic ^{3}He and ^{14}C methods with implications for excess ^{40}Ar, Geology 22 (1994) 135–138.

[71] J.M. Liccardi, M.D. Kurz, P.U. Clark, E.J. Brook, Calibration of ^{3}He production rates from Holocene lava flows in Oregon, USA, and effects of the Earth's magnetic field, Earth Planet. Sci. Lett. 172 (1999) 261–271.

[72] R.P. Ackert, B. Singer, H. Guillou, M.R. Kaplan, M.D. Kurz, Long-term ^{3}He production rates from ^{40}Ar/^{39}Ar and K–Ar dated Patagonian 47°S, Earth Planet. Sci. Lett. 210 (2003) 119–136.